Cerebral Cortex, November 2015;25: 4415–4429

doi: 10.1093/cercor/bhv039
Advance Access Publication Date: 10 March 2015
Original Article

ORIGINAL ARTICLE

Synaptic Conductance Estimates of the Connection Between Local Inhibitor Interneurons and Pyramidal Neurons in Layer 2/3 of a Cortical Column

Jochen H.O. Hoffmann[1,2], H. S. Meyer[1,3], Arno C. Schmitt[1], Jakob Straehle[1], Trinh Weitbrecht[1], Bert Sakmann[1,4], and Moritz Helmstaedter[1,5]

[1]Department of Cell Physiology, Max Planck Institute for Medical Research, D-69120 Heidelberg, Germany, [2]Current address: Department of Dermatology, University of Heidelberg, D-69120 Heidelberg, Germany, [3]Current address: Department of Neurosurgery, Technical University of Munich, 81675 Munich, Germany, [4]Current address: Cortical Column in Silico Group, Max Planck Institute of Neurobiology, D-82152 Martinsried, Germany, and [5]Present address: Department of Connectomics, Max Planck Institute for Brain Research, D-60438 Frankfurt, Germany

Address correspondence to Jochen Hoffmann, Department of Dermatology, University of Heidelberg, INF 440, D-69120 Heidelberg, Germany. Email: jochen.hoffmann@mpimf-heidelberg.mpg.de; Moritz Helmstaedter, Department of Connectomics, Max Planck Institute for Brain Research, Max-von-Laue-Str. 4, D-60438 Frankfurt, Germany. Email: mh@brain.mpg.de

Abstract

Stimulation of a principal whisker yields sparse action potential (AP) spiking in layer 2/3 (L2/3) pyramidal neurons in a cortical column of rat barrel cortex. The low AP rates in pyramidal neurons could be explained by activation of interneurons in L2/3 providing inhibition onto L2/3 pyramidal neurons. L2/3 interneurons classified as *local inhibitors* based on their axonal projection in the same column were reported to receive strong excitatory input from spiny neurons in L4, which are also the main source of the excitatory input to L2/3 pyramidal neurons. Here, we investigated the remaining synaptic connection in this intracolumnar microcircuit. We found strong and reliable inhibitory synaptic transmission between intracolumnar L2/3 *local-inhibitor*-to-L2/3 pyramidal neuron pairs [inhibitory postsynaptic potential (IPSP) amplitude −0.88 ± 0.67 mV]. On average, 6.2 ± 2 synaptic contacts were made by L2/3 *local inhibitors* onto L2/3 pyramidal neurons at 107 ± 64 µm path distance from the pyramidal neuron soma, thus overlapping with the distribution of synaptic contacts from L4 spiny neurons onto L2/3 pyramidal neurons (67 ± 34 µm). Finally, using compartmental simulations, we determined the synaptic conductance per synaptic contact to be 0.77 ± 0.4 nS. We conclude that the synaptic circuit from L4 to L2/3 can provide efficient shunting inhibition that is temporally and spatially aligned with the excitatory input from L4 to L2/3.

Key words: GABAergic synapse, interneuron, modeling, sensitivity analysis, shunting inhibition

Introduction

Inhibitory connections contribute to postsynaptic non-linear dendritic computation and plasticity (Llinas et al. 1968; Miles et al. 1996; Larkum et al. 1999). The relevance of these connections for the shaping of sensory representations in neocortex has been demonstrated for several cortical areas including the visual, olfactory, and auditory system (Rose and Blakemore 1974;

Sillito 1975; Pollak et al. 2002; Wu et al. 2008; Poo and Isaacson 2009; Liu et al. 2011; Adesnik et al. 2012; for a review, cf. Isaacson and Scanziani 2011). In the supragranular layers of the somatosensory cortex, action potential (AP) responses to sensory stimuli are especially sparse in L2/3 pyramidal neurons in vivo ("sparse" coding, Brecht et al. 2003; Celikel et al. 2004; de Kock et al. 2007; Kerr et al. 2007), despite the strong and reliable excitatory input L2/3 receives from L4 (Feldmeyer et al. 2002; Silver et al. 2003). It was found that GABAergic inhibitory neurons are numerous in supragranular layers in rat barrel cortex (Meyer et al. 2011). Therefore, it is critical to quantitatively understand how L2/3 interneurons contribute to the low AP spiking in L2/3 pyramidal neurons upon sensory stimuli.

The relevant L4-to-L2/3 microcircuit is composed of excitatory and inhibitory pathways that are activated by L4 spiny neurons following whisker deflection and that both converge onto L2/3 pyramidal neurons (Fig. 1*D*). The excitatory pathway of this microcircuit consists of L4 spiny neurons innervating L2/3 pyramidal neurons (Feldmeyer et al. 2002). The inhibitory pathway consists of L4 spiny neurons targeting L2/3 interneurons (Helmstaedter et al. 2008). These, in turn, target L2/3 pyramidal neurons. Previous reports showed that activation of subgroups of readily excitable L2/3 interneurons from L4 is very effective (Helmstaedter et al. 2008). These L2/3 interneurons can thus contribute substantially to the shaping of the precise temporal pattern of AP spiking in L2/3 pyramidal neurons.

In the present study, we therefore used in vitro paired recordings to characterize the connection between axonally defined locally projecting L2/3 interneurons ("L2/3 local inhibitors," Helmstaedter et al. 2009b) and L2/3 pyramidal neurons in the same column. While inhibitory synaptic connections within L2/3 have been studied (Thomson et al. 1996, 2002; Reyes et al. 1998; Gupta et al. 2000; Holmgren et al. 2003; Xu and Callaway 2009; Avermann et al. 2012; Pfeffer et al. 2013), knowledge on the absolute strength of synaptic conductance for precisely defined interneuron types is still missing. Dendritic computations were shown to be highly nonlinear and to critically depend on the precise location of synaptic contacts on the dendritic tree (Behabadi et al. 2012; Gidon and Segev 2012; Jadi et al. 2012). To obtain data for realistic quantitative models of the L4-to-L2/3 microcircuit, it was thus crucial to record not only synaptic transients, but also to determine the number and location of synaptic contacts per cell pair. This allowed us to obtain estimates of inhibitory synaptic conductance strength using an inverse compartmental modeling approach. With this we can provide the missing quantitative circuit data required for mechanistic models of the L4-to-L2/3 circuit within a cortical column.

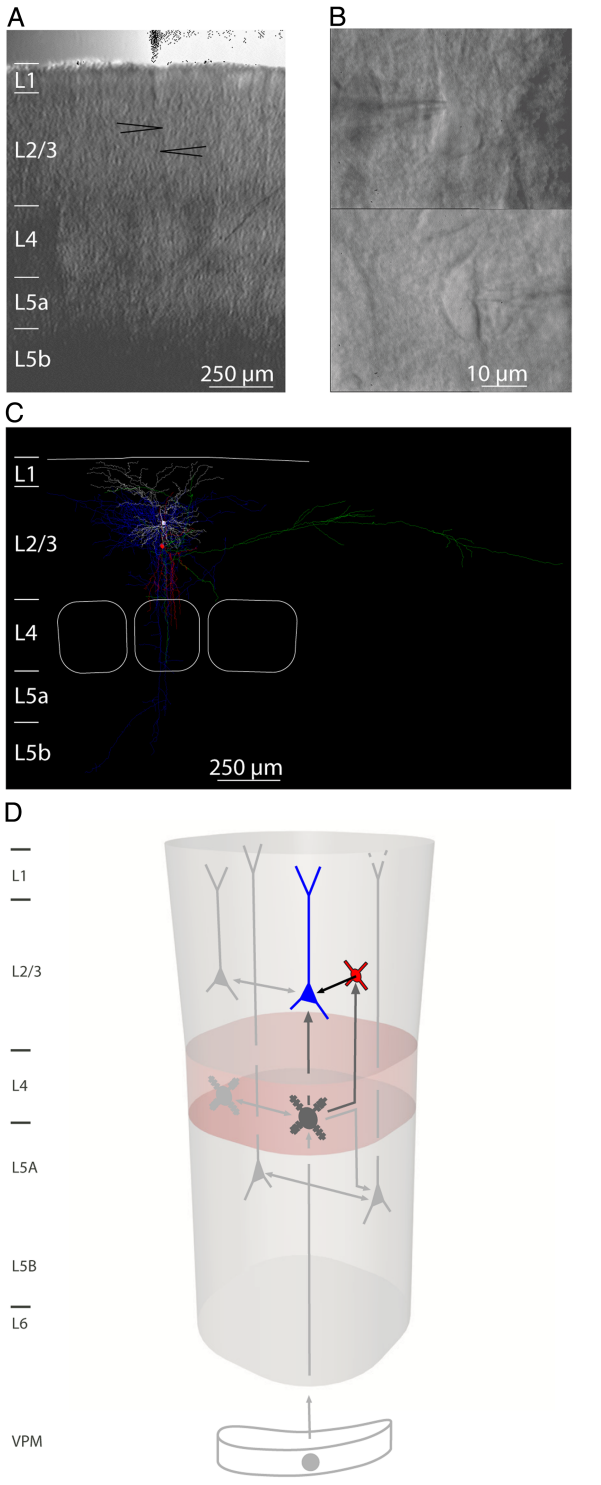

Figure 1. Paired whole-cell recordings of L2/3 pyramidal neurons and L2/3 interneurons. (*A*) Bright field image of the barrel field prior to recording. Positions of recorded cells are depicted by black arrows. (*B*) High-magnification DIC images of the pre- (bottom picture) and postsynaptic (upper picture) neuron. (*C*) Computer-aided reconstruction of soma, dendrites, and axon of the presynaptic (L2/3 interneuron, red, red, and blue) and postsynaptic (L2/3 pyramidal neuron, white, white, and green) neurons. (*D*) Schematic drawing of the L4-to-L2/3 microcircuit. The connection between L2/3 interneurons (red) and pyramidal neurons (blue) was characterized in this study. Previous studies by Feldmeyer et al. (1999, 2002, 2005, 2006) and Helmstaedter et al. (2008) characterized the intracolumnar connections shown in gray.

Methods

Preparation, Solutions

All experimental procedures were performed according to the German Animal Welfare Act. Wistar rats (19–22 days old, both sexes) were anesthetized with isoflurane and decapitated. The brain was removed and slices of somatosensory cortex were cut in ice-cold extracellular solution containing 6–7 mM $MgCl_2$/1 mM $CaCl_2$ at 350 µm thickness in a thalamocortical plane [for a detailed description, see Agmon and Connors (1991)] with minor modifications (Feldmeyer et al. 1999; Helmstaedter et al. 2008) using a vibrating microslicer (Slicer HR-2; Sigmann Elektronik, Hueffenhardt, Germany). Slices were subsequently incubated for 30–45 min in extracellular solution at 22–24 °C. In some experiments ($n = 6$), brains were incubated at 35 °C for

30 min as in Frick et al. (2007). Inhibitory postsynaptic potential (IPSP) amplitude, AP–IPSP latency, 20–80% rise time, and decay time constant were not significantly different between both preparations (one-way ANOVA). During recording, slices were continuously superfused with an extracellular solution containing (in mM): 125 NaCl, 25 $NaHCO_3$, 2.5 KCl, 1.25 NaH_2PO_4, 2 $CaCl_2$, 1 $MgCl_2$, and 25 glucose (equilibrated with 95% O_2 and 5% CO_2). The pipette (intracellular) solution contained (in mM): 135 K-gluconate, 10 HEPES, 10 phosphocreatine, 4 KCl, 4 ATP-Mg, and 0.3 GTP (adjusted to pH 7.2 with KOH). Biocytin (Sigma, Munich, Germany) at a concentration of 4–6 mg/mL was added to the pipette solution, and cells were filled during 1–2 h of recording.

Identification of Barrels

Slices were placed in the recording chamber under an upright microscope (Axioskop, Carl Zeiss, Göttingen, Germany) and inspected at low magnification (×5/0.15 NA) using bright-field illumination. Barrels were identified as >2 light "hollows" in L4 separated by dark bands. The barrel field was photographed for later analysis.

Electrophysiological Recordings

Interneurons were searched in L2/3 above barrels using a water ×60/0.90 NA objective and infrared differential interference contrast (IR-DIC) microscopy (Dodt and Zieglgansberger 1990; Stuart et al. 1993). The intrinsic electrical excitability of the interneuron was then recorded using rectangular current pulses of 500 ms length and varying amplitude [similar to Helmstaedter et al. (2009a); for details see below]. Pyramidal neurons in L2/3 were patched with a second pipette (Fig. 1A,B). APs were then elicited in the interneuron to test for synaptic connections. To capture small IPSPs, pyramidal neurons were depolarized to −50 to −60 mV during the connection test and the response was averaged over at least 18 sweeps. After recording, the pipettes were positioned above the recorded cells, and the barrel pattern was again photographed at low magnification using bright-field illumination. All recordings were performed in whole-cell configuration at 32–36 °C.

Histological Procedures

After recording, slices were fixed at 4 °C for at least 24 h in 100 mM PBS, pH 7.4, containing 4% paraformaldehyde. Slices containing biocytin-filled neurons were processed using a modified protocol described previously (Lübke et al. 2000). Slices were incubated in 0.1% Triton X-100 solution containing avidin-biotinylated horseradish peroxidase (ABC-Elite-Kit; Camon, Wiesbaden, Germany); subsequently, they were reacted using 3,3-diaminobenzidine as a chromogen under visual control until the dendritic and axonal arborization was clearly visible. Slices were then mounted on slides, embedded in Mowiol (Kuraray Specialities Europe, Frankfurt am Main, Germany), and enclosed with a coverslip.

Reconstructions and Morphological Analysis

Three-dimensional reconstructions of biocytin-labeled pairs were made using the Neurolucida software (MicroBrightField, Colchester, VT, USA) and an Olympus Optical (Hamburg, Germany) BX51 microscope at a final magnification of ×1000 using a ×100, 1.25 NA objective (Fig. 1C). The reconstructions were used to construct average length–density maps of the pre- and postsynaptic axons and dendrites. Pairs were then classified according to the axonal projection *type* of the presynaptic L2/3

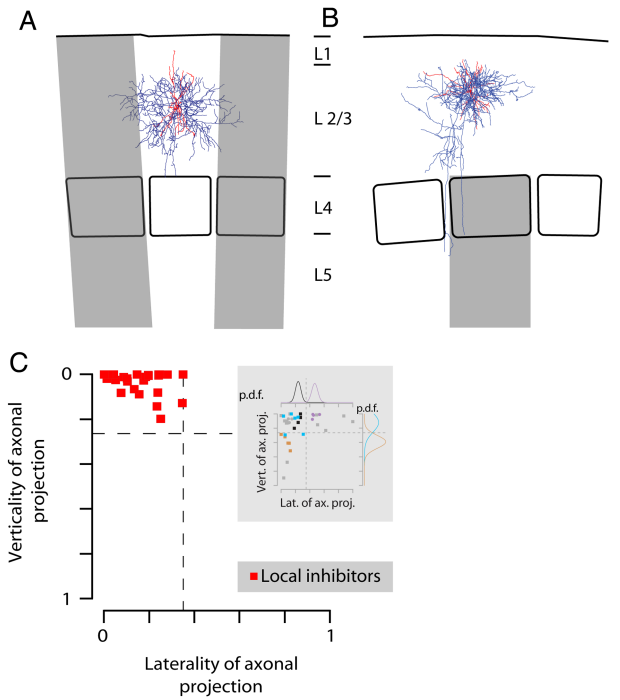

Figure 2. Quantitative analysis of the axonal projection domains. (*A*) Reconstruction of a L2/3 interneuron (soma and dendrites, black; axon, blue) from rat barrel cortex. Home column, white; area beyond home column and adjacent septa, gray. The laterality was defined as a linear combination of the ratio of axonal path length extending beyond the home column and the total lateral axonal extent (90% of the axonal length density, cf. Methods) extending beyond the home column in units of home-column width. (*B*) Reconstruction of a L2/3 interneuron from barrel cortex. Color code as above. The verticality was defined as the ratio of axonal path length extending vertically beyond the upper border of L4. (*C*) Distribution of axonal laterality and verticality for 26 *local inhibitor* interneurons (red). Maximum laterality and verticality of the axonal projection (laterality of axonal projection and verticality of axonal projection, respectively) for *local inhibitors* were derived from the probability density function (p.d.f.) of laterality and verticality of interneuron groups in a study by Helmstaedter et al. (2009a). An inset shows the axonal laterality and verticality of interneurons examined in this latter study (cf. Methods and Results; inset: *local inhibitor group* 1, black; *lateral inhibitor group* 1, purple; *local inhibitor group* 3, light blue; *feedback inhibitor group* 1, orange).

interneuron with respect to the home barrel column (Fig. 2; cf. Results and Discussion; Helmstaedter et al. 2009b). A maximum value of 0.35 for axonal "laterality" was defined to separate "local" from "lateral" interneurons. This value corresponds to the intersection between the normal distributions of axonal laterality of the most similar *local* and *lateral inhibitor group* [*local inhibitor group* 1 and *lateral inhibitor group* 1; for a detailed description of interneuron groups, see Helmstaedter et al. (2009a)]. The same method was applied to calculate a maximum "verticality" of 0.26 (*local inhibitor group* 3 and *translaminar inhibitor group* 1). Only pairs with complete staining of the dendrites and axons were chosen for identification of putative synaptic contacts. Potential contacts were identified as a close apposition of a presynaptic axon and the postsynaptic dendrite in the same focal plane, visualized at ×1000 magnification (cf. Feldmeyer et al. 2002).

Intrinsic Electrical Excitability

Rectangular current pulses of 500 ms duration and varying amplitude were injected into the soma of the interneuron (cf. Fig. 3). From these traces, 5 parameters were quantified as described previously (Helmstaedter et al. 2009a): (1) AP frequency

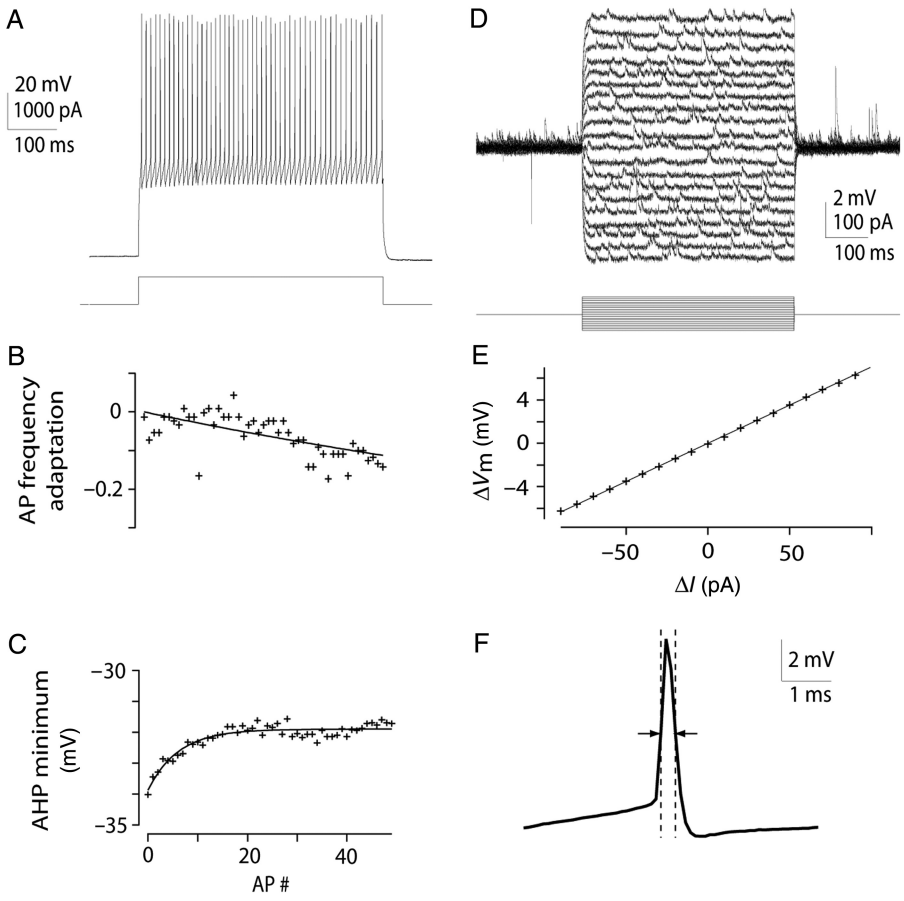

Figure 3. Quantification of intrinsic electrical parameters. (*A*) AP discharge pattern of a *local inhibitor* evoked by somatic injection of a 500-ms current pulse. The trace with an initial frequency closest to 100 Hz (interspike-interval of ~10 ms) was chosen for further analysis. (*B*) AP frequency adaptation, measured as ratio between the initial and last frequency on a mono-exponential fit to the frequencies in the AP train shown in (*A*). (*C*) AP AHP minimum voltages in the AP train shown in (*A*). The offset between the first and the last AHP minimum voltage on a mono-exponential fit to the AHP minimum voltages was calculated as AHP minimum voltage adaptation. (*F*) AP half width of the first AP in the AP train shown in (*A*). (*D*) Membrane voltage responses of the same interneuron to subthreshold current injections at resting membrane potential. (*E*) *I*/*V* ratio corresponding to (*D*). The *I*/*V* ratio was used to constrain the somatic input resistance at resting membrane potential (cf. Methods).

adaptation ratio (Fig. 3*B*), measured as offset between the initial and last frequency on a mono-exponential fit to the frequencies in the AP train for which the initial frequency was closest to 100 Hz (100 Hz trace, Fig. 3*A*), (2) AP after-hyperpolarization (AHP) minimum voltage adaptation, measured as the offset between the first and the last AHP minimum voltage on a mono-exponential fit to the AHP minimum voltages in the 100-Hz trace (Fig. 3*C*), (3) the AP half width of the first AP in the 100-Hz trace (Fig. 3*F*), (4) AP firing threshold, and (5) somatic input resistance at resting membrane potential, measured as *I*/*V* ratio (Fig. 3*D*,*E*).

Analysis of Postsynaptic Potentials

APs were elicited in the interneuron and the subsequent PSP changes in the pyramidal neuron were recorded. PSPs that were hyperpolarizing at the holding potential of −50 to −60 mV were classified as IPSPs. Unitary PSP properties were determined as described previously (Feldmeyer et al. 1999) with some modifications for the analysis of IPSPs. Briefly, a putative IPSP peak was determined within a "peak search window" of 6–18 ms after the presynaptic AP, and the IPSP amplitude was averaged over a 0.8-ms window (0.3 ms before and 0.5 ms after the determined peak time). Subsequently, a baseline potential measured in a 5-ms window just preceding the IPSP was subtracted. Failures were detected as events with amplitudes of <1.5 times the baseline noise within the baseline window or with latencies exceeding the average latency by >1.5 ms. To compensate for sweeps that were incorrectly classified as failures due to very small IPSP amplitudes, a corrected failure rate (fr_{corr}) was calculated for each connection. First, all sweeps that were classified as failures ($n_{failures}$) were averaged (averaged failure trace, aft) and analyzed as described above to determine the IPSP amplitude in that trace [$IPSP_{Amp}$(aft)]. Examples of failures, successful transmissions, an average failure trace, and an average trace of all sweeps for a weak connection (−0.23 mV IPSP amplitude) are given in Supplementary Figure 7. The ratio of the IPSP amplitude in the average failure trace [$IPSP_{Amp}$(aft)] to the IPSP amplitude in an average trace of all sweeps ($IPSP_{Amp}$) was assumed to approximate the ratio of incorrectly classified failures. Thus, the fr_{corr} was calculated as

$$fr_{corr} = \frac{\left(n_{failures} * \left(1 - \frac{IPSP_{amp}(aft)}{IPSP_{amp}}\right)\right)}{n_{sweeps}} \quad (1)$$

The time points at which the IPSP attained 20% and 80% of the total IPSP amplitude were determined on a parabolic fit to the initial and final IPSP rise phase, respectively. The difference between these time points was recorded as 20–80% rise time. The

decay was mono-exponentially fitted in a 50- to 70-ms window starting 5 ms after the IPSP peak.

Paired-pulse ratios were determined from averaged traces. Recordings were made at different holding potentials, and a weighted linear fit for at least 3 holding potentials around the resting membrane potential was used to constrain the synaptic reversal potential. De- and hyperpolarizing rectangular current pulses of 500 ms length were used to estimate the membrane time constant (τ_m). Subthreshold *I–V* curves were fitted assuming a quadratic relation between injected current and the resulting voltage deflection, enabling prediction of R_{in} over a broad voltage range (Waters and Helmchen 2006). AP discharge patterns were quantitatively analyzed offline [for details, see Helmstaedter et al. (2009b)]. Corrections for series resistance were done offline for all recordings.

Simulations

Ten pairs for which all previous analyses could be completed were chosen for simulation. Neurolucida reconstructions were converted to a format readable by NEURON using custom-written procedures (cf. Helmstaedter et al. 2009b). Modeling was performed using NEURON 5.8 (Hines and Carnevale 1997). Fitting was done with NEURON using the principal axis method (Brent 1973) for parameter searching. Parameters were determined for each neuron individually. R_i was assumed to be 150 Ωcm based on previous studies (Trevelyan and Jack 2002; Sarid et al. 2007). For this R_i, the membrane resistance at the holding potential ($R_{m,Ehold}$) and at the resting membrane potential ($R_{m,Erest}$) were optimized to fit the experimental R_{in} at the holding potential and resting membrane potential, respectively. C_m was calculated as $R_{m,Erest}$/experimental τ_m. Spines were inserted into the dendrites by modifying the physical dimensions (diameter, *d*, and length, *l*) of each dendritic section as in Stratford et al. (1989):

$$F = (A_{sh} + A_{sp})/A_{sh}, \tag{2}$$

$$d' = d * F^{1/3}, \tag{3}$$

$$l' = l * F^{2/3}, \tag{4}$$

with A_{sh} the area of the shafts and A_{sp} the area of the spines.

The area of each spine in μm^2 and spine density per μm dendritic length were assumed to be 1 and 0.97, respectively (Lübke et al. 2003).

Inhibitory synaptic conductance g_{syn} (nS) at the contact site was modeled as:

$$g_{syn}(t) = g_{syn,max} * c_1 \left(c_2 * \left(e^{-\frac{t}{\tau_{decay}1}} - e^{-\frac{t}{\tau_{rise}}} \right) + (1 - c_2) * e^{-\frac{t}{\tau_{decay}2}} \right), \tag{5}$$

with a dimensionless constant c_2 ranging from 0 to 1, and a constant c_1 defined so that the peak conductance equals $g_{syn,max}$ (cf. Supplementary Table 1 for further details on the implementation of the above equation in NEURON). The synaptic reversal potential was set to fit the experimentally observed reversal potential. Minimization of the mean squared error between the model output and the averaged experimentally recorded somatic IPSP in 2 fitting windows at the most depolarized potential served as target function to optimize the synaptic parameters:

$$L = \frac{\sum_{t=t_1}^{t_1+n_1*dt} (v_{m,sim}(t) - v_{m,exp}(t))^2 + 2\sum_{t=t_2}^{t_2+n_2*dt} (v_{m,sim}(t) - v_{m,exp}(t))^2}{n_1 + n_2} \tag{6}$$

with t_1, n_1 and t_2, n_2, onset and duration of the first and second fitting window, respectively. Weighted fitting windows were chosen to obtain equally good fits to the early (first 15–20 ms) and late phase of the IPSP. On average, the double-weighted fitting window (t_2, n_2) to the postsynaptic IPSP began 3 ± 0.4 ms (range 3–4) after the presynaptic AP and had a duration of 15 ± 7 ms (range 10–37); the single-weighted window (t_1, n_1) began 19 ± 7 ms (range 15–40) after the AP and had a duration of 63 ± 14 ms (range 30–80).

For all data, mean ± SD are given.

Results

Whole-cell recordings from pairs of L2/3 interneurons and L2/3 pyramidal neurons were made in acute slices of rat barrel cortex (Fig. 1*A*,*B*). Barrel outlines in L4 were used to delineate the borders of putative cortical columns. Only cell pairs with both the presynaptic interneuron and the postsynaptic pyramidal neuron located in L2/3 of the same column were investigated. Figure 1*C* shows the reconstruction of the pair shown in Figure 1*A*,*B*. The L2/3 interneuron axon (shown in blue in Fig. 1*C*) was largely confined to the home column including the septa. The interneuron dendrites (shown in red in Fig. 1*C*) extended to L2/3 and the upper half of L4.

L2/3 interneurons were classified into axonal projection types with reference to cortical columns as previously reported (cf. Discussion; Helmstaedter et al. 2009a, 2009b). In face of varying interneuron classifications (e.g., Karube et al. 2004; Markram et al. 2004; Ascoli et al. 2008; DeFelipe et al. 2013), we focused on the axonal projection with reference to functional cortical units as the key classification criterion since it directly predicts synaptic innervation within and across presumed cortical modules. One possible quantitative method to further subclassify interneurons based on morphological, intrinsic electrical, and functional anatomical properties was reported by Helmstaedter et al. (2009a). The results of this subclassification are presented in Supplementary Methods, Results, and Discussion, Supplementary Figures 1–3, and Supplementary Tables 2–6.

Identification of L2/3 Interneuron Axonal Projection *Type*

The axonal projection *type* of the presynaptic interneuron was determined based on the distribution of axonal path length with reference to the layers and borders of the home column (Fig. 2, cf. Methods and Helmstaedter et al. 2009b for details). Briefly, laterality of the axonal projection was quantified as the linear combination of the ratio of axonal path length beyond the lateral borders of the home column including the septa and the horizontal extent of axonal path length in units of width of the home column in L2/3 including half of the septa (Fig. 2*A*). Verticality was quantified as the ratio of axonal path length extending to regions below L2/3 (gray shaded area in Fig. 2*B*). Figure 2*C* shows the distribution of laterality and verticality for the 26 *local inhibitors*, defined as interneurons with *laterality* <0.35 and *verticality* <0.26 based on the classification previously made in an unbiased population of L2/3 interneurons (Fig. 2*C*, inset; cf. Methods; Helmstaedter et al. 2009a).

Dendritic and Intrinsic Electrical Properties

The dendritic geometry of most *local inhibitors* would be qualitatively described as "multipolar" (Fig. 2). The *local inhibitors* shown in Figure 2*A*,*B* had 5 and 8 primary dendrites with a total length of 2.6 and 2.8 mm, respectively. On average, *local inhibitors* had 8.0 ± 2 dendrites with a total length of 3.1 ± 0.6 mm ($n = 26$). A gallery of all 26 *local inhibitor* morphologies is provided in Supplementary Figure 3. Figure 3*A* shows the AP discharge pattern of a *local inhibitor* upon somatic injection of a 500-ms current pulse. Figure 3*D* shows membrane voltage responses of the same interneuron to subthreshold current injections. These firing patterns would match the often-used description "fast spiking."

Using these electrical recordings, 5 parameters were quantified as described previously (Helmstaedter et al. 2009a, cf. Methods): (1) AP frequency adaptation ratio (Fig. 3*B*), (2) AP AHP minimum voltage adaptation (Fig. 3*C*), (3) the AP half width of the first AP in the 100-Hz trace (Fig. 3*F*), (4) AP firing threshold, and (5) somatic input resistance at resting membrane potential, measured as *I*/*V* ratio (Fig. 3*D*,*E*). On average, the AP frequency adaptation ratio was −0.11 ± 0.21, the AHP minimum voltage adaptation was 1.9 ± 1.7 mV, the AP half width was 0.39 ± 0.2 ms, the AP firing threshold was −42.9 ± 5.7 mV, and the somatic input resistance was 73 ± 31 MΩ. Note, however, that the AP discharge properties of *local inhibitors* were very heterogeneous (range: −0.68 to 0.34, −1.2 to 6.2 mV, 0.25 to 0.83 ms, −54 to −24 mV, and 34 to 168 MΩ, for the 5 latter properties, respectively).

Synaptic Properties

After classification of L2/3 interneurons, the synaptic properties of the L2/3 *local inhibitor*-to-L2/3 pyramidal neuron connections were analyzed. Figure 4*A*–*D* shows data from a single connection. First, average unitary IPSP properties were determined at a depolarized postsynaptic potential (approximately−55 mV, Figure 4*A*,

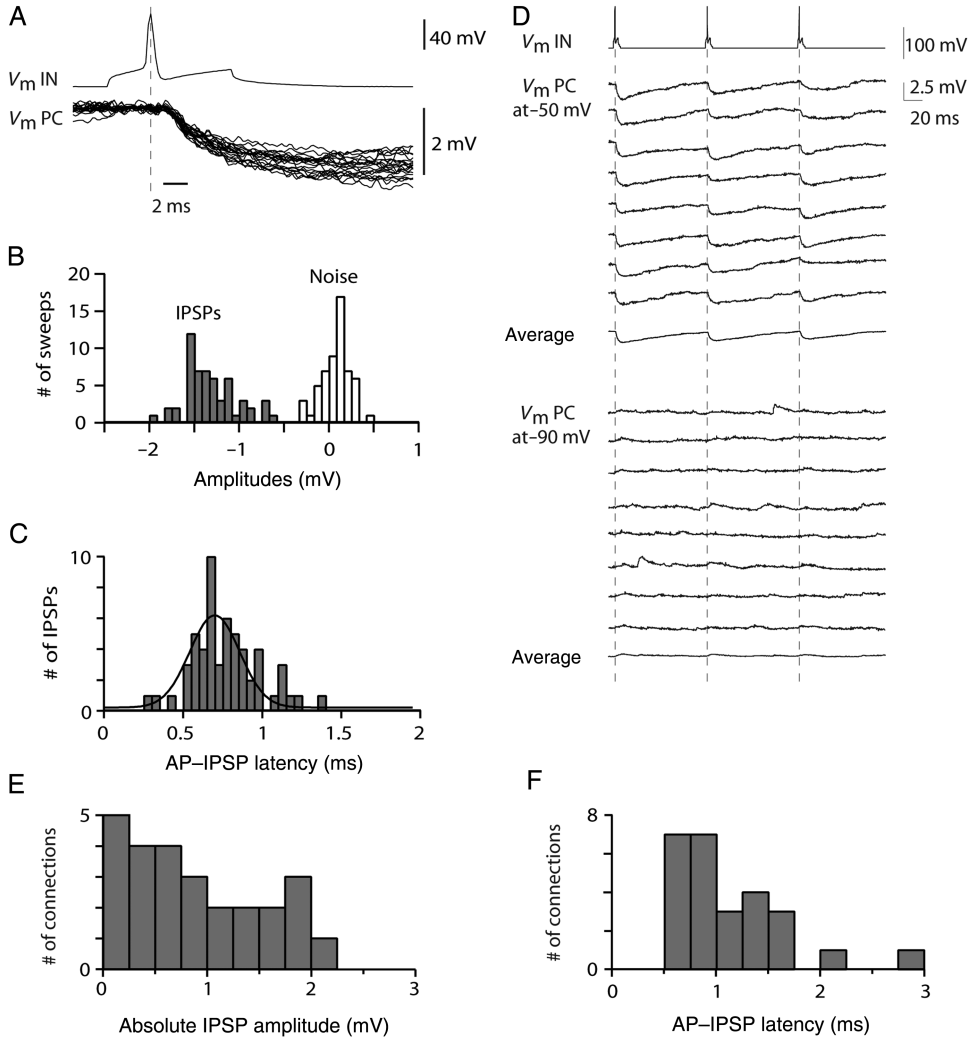

Figure 4. Properties of IPSPs in the *local inhibitor*-to-L2/3 pyramidal neuron connections. (*A*) Presynaptic AP and overlay of 20 successive postsynaptic IPSPs at a postsynaptic holding potential of −50 mV for the pair shown in Figure 6*A*. (*B*) IPSP unitary amplitude histogram for this connection. The unitary IPSP amplitudes (gray) of this pair were on average −1.75 ± 0.27 mV ($n = 56$ sweeps) and could be readily distinguished from noise (white). (*C*) AP–IPSP onset latency histogram for this connection. The AP–IPSP onset latency of this pair was on average 0.74 ± 0.17 ms. A Gaussian fit demonstrates the narrow distribution. (*D*) Train of 3 presynaptic APs at 10 Hz (top trace) and 8 consecutive sweeps at a postsynaptic holding potential of −50 mV (middle traces). The PSPs were on average hyperpolarizing and depressing in amplitude (middle trace). Eight consecutive sweeps at a hyperpolarized postsynaptic holding potential of −90 mV (bottom traces). The PSPs were depolarizing on average (bottom trace). All recordings were performed using a "low chloride" internal solution (4 mM Cl^-). (*E* and *F*) Histograms of IPSP amplitudes and AP–IPSP onset latencies for all 26 *local inhibitor*-to-L2/3 pyramidal neuron connections, respectively.

bottom trace and Figure 4D, top traces); measurements were made using a "low chloride" internal solution (4 mM Cl^-) to maintain assumedly physiological Cl^- concentrations (cf. Methods). The presynaptic interneuron was stimulated at a frequency of 10 Hz. The IPSP amplitude of the pair shown in Fig. 4A–D was on average −1.75 ± 0.27 mV ($n = 56$ sweeps) and could be readily distinguished from noise (Fig. 4B). The AP–IPSP latency was 0.74 ± 0.17 ms (Fig. 4C). IPSP amplitudes were also measured at hyperpolarized holding potentials to extract the synaptic reversal potential (Fig. 4D, bottom traces, −90 mV holding potential).

Figure 4E shows a histogram of the IPSP amplitudes of the *local inhibitor*-to-L2/3-pyramidal-cell connections. The IPSP amplitudes of *local inhibitors* showed a broad distribution that could not be explained by the variability of postsynaptic baseline potentials among experiments (mean IPSP amplitude −0.88 ± 0.67 mV, average baseline potential −57 ± 4 mV, Pearson correlation 0.2, $P = 0.4$, $n = 26$, cf. Supplementary Fig. 4). The average 20–80% rise time and decay time constants were 3.5 ± 0.8 ($n = 26$) and 76 ± 53 ms ($n = 26$), respectively. Figure 4F shows a histogram of the AP–IPSP onset latencies in the *local inhibitor*-to-L2/3 pyramidal neuron connections. On average, AP–IPSP latencies were 1.1 ± 0.5 ms ($n = 26$), ranging from 0.6 to 2.8 ms for individual connections. Presynaptic APs reliably evoked IPSPs with a low average failure rate of 7.9 ± 14% ($n = 26$). This number represents the failure rate corrected for successful transmissions misclassified as failures (cf. Methods). The uncorrected failure rate was 10.7 ± 17% ($n = 26$). In 65% (17 of 26) of pairs, synaptic transmission never failed at all (18 to 56 sweeps per pair).

In 6 pairs, IPSP amplitudes around resting potential [−75 ± 3 mV ($n = 6$)] were large enough for quantitative analysis and found to be 0.23 ± 0.1 mV. This number represents an upper estimate, as IPSP amplitudes at holding membrane potential of approximately −55 mV in these 6 cells were larger than the total average of respective IPSPs in all other local inhibitors (−1.2 vs. −0.88 mV).

Intersoma distance was not significantly associated with the number of contacts or IPSP amplitudes in the present study (Spearman correlation coefficient = −0.117, $P = 0.654$, $n = 17$ and −0.127, $P = 0.537$, $n = 26$, respectively). Reciprocal connections were found in 16 of 22 cells tested (73%). EPSP amplitudes were 0.77 ± 0.8 mV on average and were not correlated to IPSP amplitudes (Spearman correlation coefficient = −0.08, $P = 0.772$, $n = 16$).

Short-Term Synaptic Dynamics

Figure 5A shows 3 consecutive postsynaptic IPSPs evoked by presynaptic APs at 10 Hz stimulation frequency. In the connection shown, the paired-pulse ratio was 0.68 for the second to first and 1 for the third to second IPSP at 10 Hz. Paired-pulse ratios at 10 and 40 Hz AP frequency for all L2/3 *local inhibitors* are shown in Figure 5B,C. Of 26 pairs, 23 showed on average short-term depression [average paired-pulse ratios: 0.78 ± 0.38 and 1.02 ± 0.53 ($n = 26$) for first to second AP and second to third AP at 10 Hz, respectively; 0.64 ± 0.29 and 0.85 ± 0.37 ($n = 19$) at 40 Hz]). Paired-pulse ratios (10 and 40 Hz) of individual pairs were determined from an average of 27 (range 18–56) and 20 (range 15–20) sweeps, respectively.

Synaptic Contacts

Figure 6A shows a light microscopic image of a synaptically connected pair of a L2/3 *local inhibitor* and a L2/3 pyramidal neuron. Six putative synaptic contacts were found (indicated by black circles in Fig. 6A). Two of them were located on basal dendrites

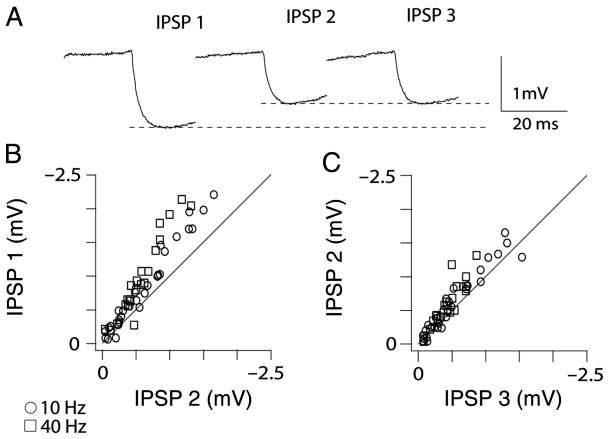

Figure 5. Short-term plasticity of *local inhibitor*-to-L2/3 pyramidal neuron connections. (*A*) Average amplitudes of 3 consecutive IPSPs at a depolarized postsynaptic potential evoked by stimulation of presynaptic APs at 10 Hz. The IPSPs in this connection were on average depressing in amplitude. (*B* and *C*) Ratio of first to second (*B*) and second to third (*C*) IPSP amplitude. Most connections were on average depressing in amplitude.

(contacts 1 and 6 in Fig. 6A) and 4 on apical oblique dendrites (contacts 2–4 and 5 in Fig. 6A; see Fig. 6B1–B6 for images at higher magnification). The presynaptic axon (indicated by black arrows in Fig. 6B1–B6) was found to intersect with the postsynaptic dendrite in the same focal plane. The average number of putative contacts was 6.2 ± 2 (range 3–10, $n = 17$ pairs). The average path distance of putative synaptic contacts to the soma of the postsynaptic pyramidal neuron was 107 ± 64 μm (range: 5–354, $n = 106$ contacts; see histogram in Fig. 9). 50% of putative contacts were located on basal dendrites and 47% were located on apical oblique dendrites. Only 3 putative contacts were located on the soma. The number of contacts was positively correlated with the absolute IPSP amplitude [Fig. 6C, correlation coefficient, 0.58, $P = 0.016$, $n = 17$ (two-sided Pearson correlation)].

Innervation Domains

To quantify the L2/3 *local inhibitor*-to-L2/3 pyramidal neuron innervation probability, 2D maps of axonal (L2/3 interneuron) and dendritic (L2/3 pyramidal neuron) length density were calculated (cf. Lübke et al. 2003; Helmstaedter et al. 2009b). The axonal density map of *local inhibitors* was largely confined to the borders of the home column including septa (Fig. 6D1). Accordingly, single-cell morphologies demonstrate how axonal arborization of *local inhibitor* interneurons largely respect home-column borders (cf. Supplementary Fig. 3, e.g., pair 2008-09-25-A and pair 2008-10-28-A).

Multiplication of the respective axonal and dendritic (Fig. 6D1–2) length densities yielded a predicted map of innervation probability (Fig. 6D3). The contour containing 90% of the predicted innervation probability ("innervation domain," yellow outline in Fig. 6D3) can be interpreted as the area in which 90% of the contacts are made if the distribution of these contacts depended mainly on spatial proximity. It was strictly confined to the home column. The average path length of *local inhibitor* axon in the innervation domain was 15.5 mm with a bouton frequency of 0.3 ± 0.04 boutons per μm of axonal path length.

Synaptic Conductance Estimates

To constrain the unitary synaptic parameters underlying the observed experimental IPSPs, simulations using NEURON were

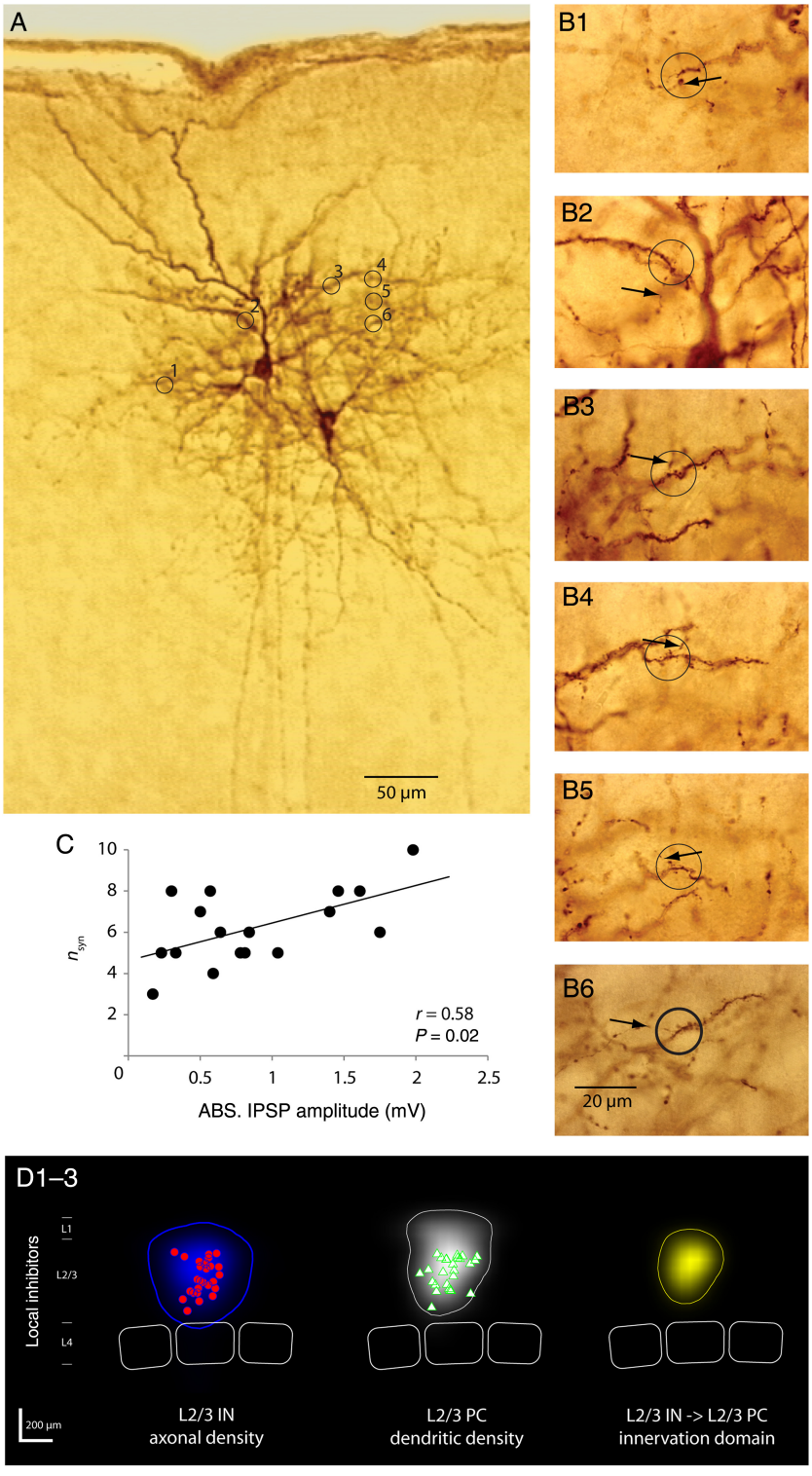

Figure 6. Light microscopic analysis of synaptic contacts and average axonal projection and innervation domain of *local inhibitor*-to-L2/3 pyramidal neuron connections. (*A*) Light microscopic image of a synaptically coupled *local inhibitor*-to-L2/3-pyramidal neuron pair at low magnification. Putative synaptic contacts made by the *local inhibitor* (lower, right neuron) are indicated by black circles and numbered from 1 to 6. (*B1–B6*) Images at higher magnification of the putative contacts 1–6 shown in (*A*). The presynaptic axon (indicated by black arrows) was found to intersect with the postsynaptic dendrite in a single focal plane. (*C*) The number of putative contacts identified using this method was significantly correlated with the IPSP amplitude of the respective connection (two-sided Pearson correlation). (*D1*) The axonal length density map of *local inhibitors* was largely confined to the borders of the home column and L2/3. (*D2*) Dendritic length–density map and soma positions of the pyramidal neurons contacted by *local inhibitors*. (*D3*) Inhibitory innervation probability map of *local inhibitors*. Inhibitory innervation probability maps were obtained by multiplication of the respective axonal (*D1*) and dendritic length densities (*D2*). The yellow contour comprises 90% of the inhibitory innervation probability (i.e., "innervation domain"). The innervation domain can be interpreted as the area in which 90% of the contacts are made if the distribution of these contacts depended mainly on spatial proximity. The blue and white contours in *D1–2* comprise 90% of respective length–density.

made for 10 synaptically connected *local inhibitor*-to-pyramidal neuron pairs. The unknown synaptic parameters were: synaptic reversal potential (E_{syn}), maximum synaptic conductance ($g_{syn,max}$), and synaptic time constants (τ_{rise}, τ_{decay1}, and τ_{decay2}). For each connection, a detailed compartmental model of the postsynaptic pyramidal neuron was built using (1) the reconstruction of the postsynaptic pyramidal neuron soma and dendrites, (2) passive membrane properties (membrane capacitance C_m, membrane resistance R_m, and axial resistance R_a), calculated from the measured input resistance and membrane time constant (cf. Methods), (3) synapses, inserted at the light microscopically identified putative synaptic locations (number of synapses n_{syn}; cf. Figs 6A and 7A), (4) synaptic reversal potentials (E_{syn}), and (5) synaptic conductances ($g_{syn,max}$, τ_{rise}, τ_{decay1}, τ_{decay2}, and c_2, cf. Methods). The conductance at a synaptic contact was effectively modeled as a weighted linear combination of a bi- and a mono-exponential module (cf. Methods).

Figure 7A shows a 2D projection of the reconstruction of a pyramidal neuron (cf. Fig. 6A,B), with the 6 observed putative synapses indicated by black arrows (the morphologies of all reconstructed pyramidal neurons are provided in Supplementary Data 1). The measured somatic IPSP is shown in Figure 7B (gray line). Numerical simulations were then made using the model described above. Synaptic parameters at each synaptic contact in the model were optimized such that the simulated somatic IPSP best-fitted the average measured somatic IPSP (inverse modeling and principal component method, see Methods equation 6). The model somatic IPSP using the synaptic parameters that provided the best fit between the model output and the experimentally measured somatic IPSP is shown in Figure 7B as black trace (for details of the fitting procedure, cf. Methods; experimental IPSP traces and model output for all 10 simulated pairs are given in Supplementary Fig. 5). The underlying current and voltage deflections at the 6 synaptic sites are shown in Figure 7C. Synaptic parameters in the model were assumed to be homogeneous at the 6 synaptic sites. Differences in local voltage deflections thus possibly reflected local input resistance variations (e.g., contact 2 vs. contact 1 in Fig. 7A,C).

The distribution of maximum synaptic conductances determined by this method was remarkably homogeneous (0.77 ± 0.35 nS synaptic conductance per synaptic site, range 0.13–1.15, $n = 10$, Table 2), given the considerable variability in input parameters (cf. Table 1). On average, τ_{rise} was 0.18 ± 0.06 ms, and τ_{decay1} and τ_{decay2} were 2.97 ± 1.85 and 39.49 ± 45.95 ms, respectively (further details of the modeling parameters including the weights of the individual modules are given in Supplementary Table 1).

Sensitivity Analysis

We then analyzed the sensitivity of our conductance estimates to errors in C_m, R_m, R_a, E_{syn}, and n_{syn} for 3 of the simulated cells. A single input parameter was varied at a time, all simulations were repeated, and the effect on the conductance estimate was recorded. Figure 8A shows that variation in C_m by 20% resulted in a $g_{syn,max}$ error of approximately 20%. R_a and R_m variations of 30% each resulted in $g_{syn,max}$ errors of <10%. Figure 8B shows that varying E_{syn} by 10 mV resulted in <40% overestimation of $g_{syn,max}$. Figure 8C shows the sensitivity of our simulations to the number of synapses. Each synapse was deactivated one at a time and the resulting error in $g_{syn,max}$ was estimated. An underestimation of synaptic contacts by $n = 1$ resulted in <45% overestimation of $g_{syn,max}$ (average error: 24%).

Discussion

The present study characterizes the connection between L2/3 *local inhibitor* interneurons and L2/3 pyramidal neurons in rat barrel cortex using physiological ("low chloride") intracellular

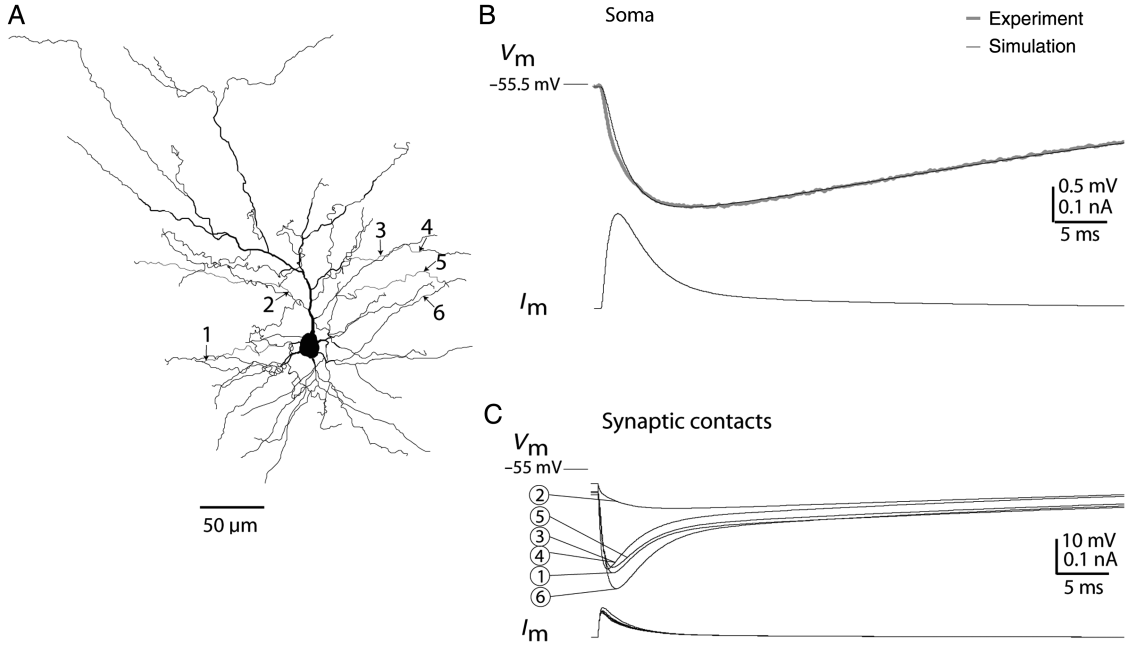

Figure 7. Extraction of synaptic parameters by fitting model to experiment. (*A*) A detailed compartmental model of the postsynaptic pyramidal neuron shown in Figure 6*A*. Six synaptic contacts (indicated by black arrows and numbered from 1 to 6) were inserted at the putative synaptic locations identified at the light microscopic level (compare Fig. 6*A*) and the synaptic parameters were optimized to fit the experimental observations (cf. Methods and Results). (*B*) Top gray trace: average somatic IPSP measured experimentally in the pair shown in Figure 6A. Top black trace: model fit using the detailed compartmental model shown in (*A*). Bottom black trace: model somatic IPSC. (*C*) Potential deflections (top traces) and currents (bottom traces) at the synaptic contacts during a simulation using the same model parameters as in (*B*).

Table 1 Input parameters for the 10 simulated cells

	Average IPSP amplitude (mV)	Holding membrane potential (mV)	Apparent syn. rev. pot. (mV)	Number of synapses	Synapse to soma distance (μm)	Input resistance[a] (MΩ)	Membrane time constant (ms)
Local inhibitors							
20050804A	−1.75	−55.5	−80.2	6	105.9	138.8	23.9
20050829A	−0.59	−63.4	−78.0	4	87.5	59.5	14.8
20050912A	−0.78	−63.6	−81.6	5	91.2	51.0	12.3
20060927A	−1.04	−55.7	−76.5	5	70.7	52.4	15.3
20061018A	−1.40	−60.1	−80.7	7	82.1	102.0	24.6
20070714A	−0.50	−57.4	−75.2	7	131.0	41.3	9.6
20070809B	−1.98	−56.3	−81.5	10	94.4	100.4	22.3
20080922A	−0.57	−56.8	−90.1	8	113.5	112.1	13.4
20080925A	−0.81	−52.6	−82.3	5	206.1	76.0	12.1
20081028A	−1.61	−55.9	−82.6	8	98.0	65.3	11.6
Average ($n = 10$)	−1.10	−57.7	−80.9	6.5	108.0	79.9	16.0
SD	0.54	3.6	4.1	1.8	38.4	31.9	5.5

Note: IPSP, inhibitory postsynaptic potential; syn. rev. pot., synaptic reversal potential.
[a]Input resistance at holding potential.

Table 2 Modeled synaptic parameters

	$g_{syn,max}$ (nS)	τ_{rise} (ms)	τ_{decay1} (ms)	τ_{decay2} (ms)
Local inhibitors				
20050804A	1.13	0.16	2.4	23.9
20050829A	0.99	0.26	2.1	18.8
20050912A	1.15	0.15	2.0	21.5
20060927A	1.01	0.25	4.0	30.0
20061018A	1.04	0.14	2.8	35.4
20070714A	0.34	0.11	7.7	169.0
20070809B	0.56	0.26	1.8	14.8
20080922A	0.13	0.13	3.2	20.9
20080925A	0.64	0.20	1.0	31.9
20081028A	0.75	0.15	2.7	28.7
Average ($n = 10$)	0.77	0.18	3.0	39.5
SD	0.35	0.06	1.9	46.0

Note: $g_{syn,max}$, maximum synaptic conductance per synaptic site; τ_{rise}, rise time constant; τ_{decay1} and τ_{decay2}, decay time constants 1 and 2.

solutions. Our main findings are: (1) L2/3 pyramidal neurons receive an on average strong and reliable intracolumnar, intralaminar input by L2/3 *local inhibitors* (IPSP amplitude −0.88 ± 0.7 mV); (2) using inverse modeling, we found an estimate of synaptic peak conductance per synaptic site of 0.77 ± 0.4 nS; (3) synaptic contacts were located at 107 ± 64 μm distance from the L2/3 pyramidal neuron soma which is within the range of the sites of excitatory synapses established by L4 spiny neurons and L2/3 pyramidal neurons.

Interneuron Classification

Interneurons can carry a wide spectrum of morphological, molecular, and electrophysiological characteristics, so that numerous classifications have been proposed (Ascoli et al. 2008; DeFelipe et al. 2013). Since these classifications do not agree yet on a relevant set of classification parameters, we chose to relate to a quantitative classification of L2/3 interneurons based on their axonal projections with reference to cortical columns, since this measure provides direct prediction of synaptic innervation. Briefly, Helmstaedter et al. (2009b) identified 3 *types* of L2/3 interneurons as *local*, *lateral*, and *translaminar* inhibitors based on their axonal projection in relation to their home column and layer using a cluster analysis. *Local inhibitors* were predicted to innervate pyramidal neurons in L2/3 of the home column. *Local inhibitors* received a strong input from L4 spiny neurons (EPSP amplitude: 0.96 ± 0.93 mV) and may therefore be substantially activated by a whisker deflection.

IPSP Properties

In many previous studies of the rat primary sensory areas, inhibitory connections were measured with "high chloride" intracellular solutions in the postsynaptic cell to facilitate the measurement of postsynaptic currents (e.g., Nicoll et al. 1996; Reyes et al. 1998; Gupta et al. 2000; Holmgren et al. 2003; Otsuka and Kawaguchi 2009; Xu and Callaway 2009) or per voltage clamp only (Packer and Yuste 2011; Pfeffer et al. 2013), which hampers a comparison with the IPSP amplitudes reported here. Other reports described intralaminar IPSP amplitudes recorded (1) by potassium methyl chloride filled sharp electrodes and elicited by unclassified L2/3 interneurons (−0.65 ± 0.44 mV, in rat somatosensory and motor cortex pyramidal neurons; Thomson et al. 2002) or by L4 and L5 fast-spiking interneurons (−1.22 ± 0.71 mV, in rat somatosensory, visual, and motor cortex pyramidal neurons; Thomson et al. 1996), and (2) by whole-cell patch clamp and elicited by L2/3 fast- and non–fast-spiking interneurons (−0.52 ± 0.11 and −0.49 ± 0.11 mV, respectively, in unclassified excitatory cells of GAD67-GFP knock-in mouse somatosensory cortex; Avermann et al. 2012). These values are within the range of the IPSP amplitudes reported here (−0.88 ± 0.67 mV).

The average 20–80% rise time and decay time constant of IPSPs were 3.5 and 76 ms for *local inhibitors*. This was considerably longer than previously reported for excitatory connections made onto L2/3 pyramidal neurons by L4 spiny neurons (20–80% rise time: 0.8 ms, decay time constant: 12.7 ms; Feldmeyer et al. 2002) and by other L2/3 pyramidal neurons (20–80% rise time: 0.7 ms, decay time constant: 15.7 ms; Feldmeyer et al. 2006). Slow kinetics of IPSPs were previously reported in studies using various techniques (e.g., Thomson et al. 1996, 2002; Holmgren et al. 2003).

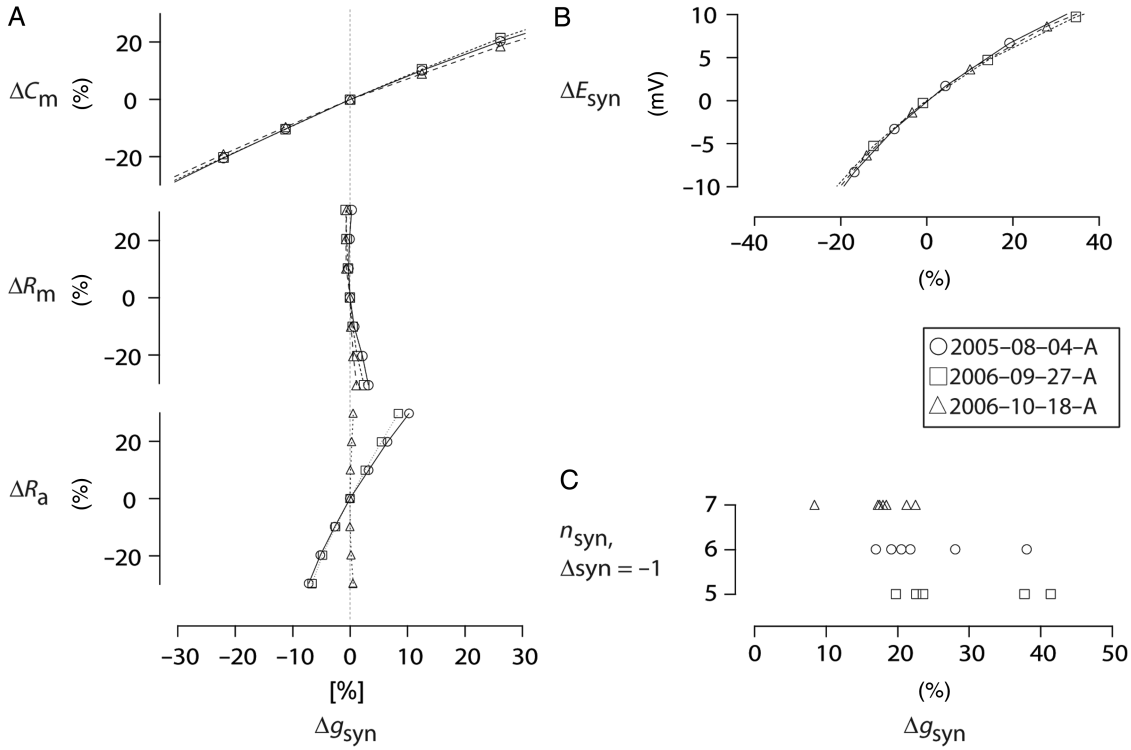

Figure 8. Sensitivity of conductance estimates to variations in other model parameters. (*A*) Sensitivity of the synaptic conductance estimates ($g_{syn,max}$) to variations in the membrane capacitance (C_m, top), membrane resistance (R_m, middle), and axial resistance (R_a, bottom). (*B*) Sensitivity of $g_{syn,max}$ to variations in the synaptic reversal potential (E_{syn}). (*C*) Sensitivity of $g_{syn,max}$ to the variations in the number of synapses (n_{syn}). Each synapse was deactivated one at a time and the resulting error in $g_{syn,max}$ was estimated.

AP half width and input resistance of interneurons were negatively correlated with the absolute IPSP amplitude in the present study (cf. Supplementary Table 7 and Supplementary Fig. 6). This is generally in line with results from a recent study by Pfeffer et al. (2013), showing that parvalbumin-positive interneurons of the mouse visual cortex, which were described to show features of fast-spiking interneurons, exhibited stronger inhibition onto pyramidal neurons than somatostatin and vasoactive intestinal peptide-positive interneurons.

Number and Positions of Contacts

Some studies reported high numbers of putative synaptic contacts in basket cell-to-pyramidal neuron connections in various layers of the somatosensory rat cortex using light microscopy (17.2; average of basket cells, Markram et al. 2004). Estimates using electron microscopy in the same cortical area, however, were considerably smaller (2.5, Thomson et al. 1996). Our data lie between these previous measurements (6.2 ± 2 contacts per connection, range 3–10, $n = 17$ pairs). The path distance of the contacts to the soma was on average 107 ± 64 µm. This soma-contact distance is larger but overlapping with the distance reported for basket cells (79 µm; average of basket cells, Markram et al. 2004), and notably not predominantly perisomatic. The criteria for basket cell definition often include a large somatic or perisomatic distribution of synaptic contacts [for a review of interneuron classifications, see Markram et al. (2004)]. In our study, however, only 3 somatic contacts could be identified at the light microscopic level (out of 106 total contacts). Synaptic contacts established using light microscopy are generally overestimated on dendrites and underestimated on the soma (Tamas et al. 1997), as some somatic contacts may not be visible due to the limited resolution in the vicinity of a heavily stained soma. However, even if some somatic contacts had to be considered, the distribution of putative synaptic contacts would remain largely dendritic. It is therefore possible that the number of somatic contacts formed by locally projecting basket cells in L2/3 of a barrel column is indeed smaller than previously estimated (Chattopadhyaya et al. 2004; quantitative estimates of perisomatic boutons of basket cells are as low as 30% including proximal dendrites).

Shunting Inhibition Versus Inhibitory Summation

The same inhibitory synaptic input can cause (1) PSP deflections toward its respective synaptic reversal potential and (2) a reduction in the postsynaptic membrane resistance, thereby creating an electric short circuit (i.e., shunting inhibition). In theory, the latter effect prevails if the synaptic reversal potential is close to the membrane resting potential and, following Ohm's law, can lead to a divisive effect on other synaptic input in spatiotemporal proximity, thereby providing regional control of dendritic computation (Rall 1964; for a review, cf. Koch 1999). To determine the precise role of shunting inhibition in a given network like the barrel cortex, it is therefore necessary to know the spatiotemporal distribution of excitatory and inhibitory inputs on the postsynaptic cell (for a review, cf. London and Hausser 2005). In the present study, the number and distribution of putative synaptic contacts made onto L2/3 pyramidal neurons by *local inhibitors* was more distal than but highly overlapping with those formed onto L2/3 pyramidal neurons by other L2/3 pyramidal neurons (2.8, 91 ± 47 µm; Feldmeyer et al. 2006) and by L4 spiny neurons (4.5, 67 ± 34 µm; Feldmeyer et al. 2002; cf. Fig. 9). Given

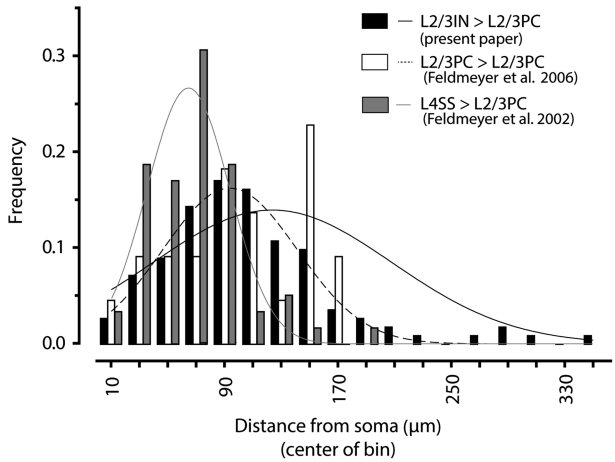

Figure 9. Location of synaptic contacts onto L2/3 pyramidal neurons by L2/3 *local inhibitors*, L4 spiny neurons, and other L2/3 pyramidal neurons. The distribution of putative synaptic contacts made onto L2/3 pyramidal neurons by *local inhibitors* (this study, black bars) is strikingly similar with the distributions of those onto L2/3 pyramidal neurons by L4 spiny neurons (gray bars) and other L2/3 pyramidal neurons (white bars) reported previously [data points and histogram adapted from Feldmeyer et al. (2002); Feldmeyer et al. (2006) for comparison]. Given a near-synchronous activation of these connections, inhibition of L2/3 pyramidal neurons might be mediated by spatial and temporal proximity of inhibitory and excitatory contacts (shunting inhibition). Relative frequency distribution and Gaussian fits are shown.

a near-synchronous activation of these connections, inhibition of L2/3 pyramidal neurons may be dominated by the effects of spatial proximity of inhibitory and excitatory contacts rather than by simple somatic summation of synaptic currents. Shunting inhibition is probably particularly important when the postsynaptic cell is close to resting membrane potential (possibly similar to the "down" state observed in vivo; Petersen et al. 2003), where IPSP amplitudes are small (−0.17 mV at −75 mV baseline potential; this study) compared with EPSP amplitudes (0.7 mV, Feldmeyer et al. 2002; 1.0 mV, Feldmeyer et al. 2006).

Compartmental ensemble simulations of the excitatory and inhibitory connections converging onto a L2/3 pyramidal neuron using realistic synaptic input may be used in future studies to demonstrate whether shunting inhibition or summation prevails in L2/3 pyramidal neurons following whisker deflection.

Anatomical Convergence

An individual *local inhibitor* had about ~4650 boutons in the innervation domain established with L2/3 pyramidal neurons (~15.5 mm axonal length in the innervation domain * average ratio of ~0.3 boutons per µm axonal length; cf. Results). Assuming that 85% of these boutons are contacting pyramidal neurons (estimated by the assumed ratio of interneurons in L2/3; Beaulieu 1993; Meyer et al. 2010), and given 6.2 synaptic contacts per *local inhibitor*-to-L2/3 pyramidal neuron connection, a single L2/3 inhibitor can make synaptic connections to approximately 640 postsynaptic L2/3 pyramidal neurons ("divergence"; connectivity ratio: 640/3000 to 4000 pyramidal neurons in L2/3 = 16–21%). Assuming that 20–80% of all L2/3 interneurons are *local inhibitors* (the broad range of this assumption reflects the lack of knowledge about the relative prevalence of axon projection-based interneuron types in the somatosensory cortex), each L2/3 pyramidal neuron would receive input from [0.15 * 640/0.85 * (0.2 . . . 0.8)] ≈ 20–90 L2/3 *local inhibitors* ("convergence").

The number of L2/3 interneurons converging onto a L2/3 pyramidal neuron is thus considerably smaller than that of L4 spiny neurons (~300–400, Lübke et al. 2003) and L2/3 pyramidal neurons (~270, Feldmeyer et al. 2006) converging onto a L2/3 pyramidal neuron. The present data on the location of inhibitory contacts suggest that approximately 125–560 [(20–90) * 6.2] inhibitory contacts from L2/3 *local inhibitors* are located on a L2/3 pyramidal neuron in close proximity to the approximately 1350–1800 [(300–400) * 4.5] (Feldmeyer et al. 2002; Lübke et al. 2003) and approximately 750 (270 * 2.8) (Feldmeyer et al. 2006) excitatory boutons from L4 spiny neurons and L2/3 pyramidal neurons, respectively. However, L2/3 interneurons have a more compact geometry than L2/3 pyramidal neurons and receive more and stronger synaptic inputs by L4 spiny neurons upon whisker deflection (L2/3 interneurons vs. L2/3 pyramidal neurons: 3-fold higher anatomical convergence and 1.8-fold higher EPSP amplitudes, Feldmeyer et al. 2002; Helmstaedter et al. 2008). Furthermore, L2/3 interneurons received a strong reciprocal input from L2/3 pyramidal neurons in the present study. It is thus likely that L2/3 interneurons are efficiently activated by L4 excitatory neurons (cf. Helmstaedter et al. 2008) and provide inhibition at the sites of excitatory input to L2/3 pyramidal neurons with only a short delay of a few milliseconds (1.1 ± 0.5 ms, this study). The peak of the inhibitory conductance transient could therefore occur in the early phase of the voltage transient in L2/3 pyramidal neurons following whisker deflection. An early activation of inhibitory connections onto L2/3 pyramidal neurons is supported by a reduction of spiking upon pre-depolarization in the early, but not in the late, phase following whisker deflection (Brecht et al. 2003).

An essential step in further unraveling inhibitory contributions is therefore the numerical simulation of the L4-to-L2/3 intracortical microcircuits. To enable such a simulation, it is crucial (1) to characterize the conductances underlying the measured potential deflections and (2) to identify the in vivo spiking pattern of L2/3 interneurons.

Modeling of Synaptic Conductances

We constrained the synaptic properties of L2/3 *local inhibitor*-to-L2/3 pyramidal neuron connections using realistic multicompartmental models. The average maximum conductance per synaptic site was found to be approximately 0.8 nS. If the single channel conductance is assumed to be approximately 20–30 pS (Brickley et al. 1999; Perrais and Ropert 1999), roughly 25–40 GABARs per synaptic site are open at the peak of the conductance transient. Previously, peak conductances have been calculated from the relation between IPSP amplitudes and holding potentials under the assumption of negligible electrotonic distance between the synaptic sites and the somatic recording site [for details, see Benardo (1994)]. Subsequent division by the number of (putative) synaptic contacts yielded an estimate for the peak synaptic conductance per synaptic site. An upper conductance estimate using this approach on our simulated cells yields (1.1 mV/23 mV/80 MΩ/6.2) ≈ 0.1 nS conductance per synaptic site. The underestimation using the analytical approach can be attributed to the significant filtering effects of fast synaptic conductance transients when measured at the soma.

The peak conductance estimates and the predicted time constants of synaptic conductance change using the inverse modeling approach presented here were remarkably similar between the 10 analyzed pairs, while the IPSP amplitudes, numbers of putative synaptic contacts, and postsynaptic electrophysiological (input resistance and membrane time constant) and

morphological properties varied substantially among the connections. Of note, the model estimates for excitatory NMDAR and AMPAR conductances are in the same range as our estimates for inhibitory synaptic conductances (0.52 ± 0.24 and 0.40 ± 0.34 nS conductance/site for AMPAR and NMDAR, respectively, Sarid et al. 2013).

The validity of inverse modeling results depends critically on the validity of the model assumptions. We therefore made a sensitivity analysis to quantify the dependence of the obtained conductance estimates to errors made in assumptions about model parameters (cf. Fig. 8). Errors in assumptions on membrane conductance, synaptic reversal potential, and number of synaptic contacts were found to have the largest impact on model predictions. Overall, however, this analysis demonstrated that the conductance estimates were rather robust with perturbations in model parameters (C_m, R_m, R_a, E_{syn}, and n_{syn}). This supports inverse modeling as a powerful tool to recover parameters that defy direct measurement (cf. also Schaefer et al. 2003, 2007, for an application of inverse modeling to conductance density estimation; and Keren et al. 2005; Druckmann et al. 2011 for inverse modeling of AP trains).

Outlook

The reliable connection between L2/3 *local inhibitors* and L2/3 pyramidal neurons as found here allows direct predictions about the strength, spatial extent, and temporal characteristics of inhibition on L2/3 pyramidal neurons in the L4-to-L2/3 microcircuit in rat barrel cortex, following a whisker stimulus. To investigate the effect of stimulus-evoked activity in the entire L4-to-L2/3 circuit, however, numerical models of this microcircuit will be required that implement the experimentally found constraints on anatomical connectivity, electrical excitability, and synaptic properties (Helmstaedter et al. 2007; Sarid et al. 2007). We suggest that such an in silico approach—when based on solid experimental data—may help to gain a mechanistic understanding of the activation of L4 and L2/3 neurons in a cortical column following a sensory stimulus.

Supplementary Material

Supplementary material can be found at: http://www.cercor.oxfordjournals.org.

Funding

The authors contributing to this article received funding by the Max Planck Society, this includes the Open Access publication charges.

Notes

Conflict of Interest: None declared.

References

Adesnik H, Bruns W, Taniguchi H, Huang ZJ, Scanziani M. 2012. A neural circuit for spatial summation in visual cortex. Nature. 490:226–231.

Agmon A, Connors BW. 1991. Thalamocortical responses of mouse somatosensory (barrel) cortex in vitro. Neuroscience. 41:365–379.

Ascoli GA, Alonso-Nanclares L, Anderson SA, Barrionuevo G, Benavides-Piccione R, Burkhalter A, Buzsaki G, Cauli B, Defelipe J, Fairen A, et al. 2008. Petilla terminology: nomenclature of features of GABAergic interneurons of the cerebral cortex. Nat Rev Neurosci. 9:557–568.

Avermann M, Tomm C, Mateo C, Gerstner W, Petersen CC. 2012. Microcircuits of excitatory and inhibitory neurons in layer 2/3 of mouse barrel cortex. J Neurophysiol. 107:3116–3134.

Beaulieu C. 1993. Numerical data on neocortical neurons in adult rat, with special reference to the GABA population. Brain Res. 609:284–292.

Behabadi BF, Polsky A, Jadi M, Schiller J, Mel BW. 2012. Location-dependent excitatory synaptic interactions in pyramidal neuron dendrites. PLoS Comput Biol. 8:e1002599.

Benardo LS. 1994. Separate activation of fast and slow inhibitory postsynaptic potentials in rat neocortex in vitro. J Physiol. 476:203–215.

Brecht M, Roth A, Sakmann B. 2003. Dynamic receptive fields of reconstructed pyramidal cells in layers 3 and 2 of rat somatosensory barrel cortex. J Physiol. 553:243–265.

Brent RP. 1973. Algorithms for minimization without derivatives. Englewood Cliffs: Prentice-Hall.

Brickley SG, Cull-Candy SG, Farrant M. 1999. Single-channel properties of synaptic and extrasynaptic GABAA receptors suggest differential targeting of receptor subtypes. J Neurosci. 19:2960–2973.

Celikel T, Szostak VA, Feldman DE. 2004. Modulation of spike timing by sensory deprivation during induction of cortical map plasticity. Nat Neurosci. 7:534–541.

Chattopadhyaya B, Di Cristo G, Higashiyama H, Knott GW, Kuhlman SJ, Welker E, Huang ZJ. 2004. Experience and activity-dependent maturation of perisomatic GABAergic innervation in primary visual cortex during a postnatal critical period. J Neurosci. 24:9598–9611.

DeFelipe J, Lopez-Cruz PL, Benavides-Piccione R, Bielza C, Larranaga P, Anderson S, Burkhalter A, Cauli B, Fairen A, Feldmeyer D, et al. 2013. New insights into the classification and nomenclature of cortical GABAergic interneurons. Nat Rev Neurosci. 14:202–216.

de Kock CP, Bruno RM, Spors H, Sakmann B. 2007. Layer- and cell-type-specific suprathreshold stimulus representation in rat primary somatosensory cortex. J Physiol. 581:139–154.

Dodt HU, Zieglgansberger W. 1990. Visualizing unstained neurons in living brain slices by infrared DIC-videomicroscopy. Brain Res. 537:333–336.

Druckmann S, Berger TK, Schurmann F, Hill S, Markram H, Segev I. 2011. Effective stimuli for constructing reliable neuron models. PLoS Comput Biol. 7:e1002133.

Feldmeyer D, Egger V, Lübke J, Sakmann B. 1999. Reliable synaptic connections between pairs of excitatory layer 4 neurones within a single "barrel" of developing rat somatosensory cortex. J Physiol. 521(Pt 1):169–190.

Feldmeyer D, Lubke J, Sakmann B. 2006. Efficacy and connectivity of intracolumnar pairs of layer 2/3 pyramidal cells in the barrel cortex of juvenile rats. J Physiol. 575:583–602.

Feldmeyer D, Lübke J, Silver RA, Sakmann B. 2002. Synaptic connections between layer 4 spiny neurone-layer 2/3 pyramidal cell pairs in juvenile rat barrel cortex: physiology and anatomy of interlaminar signalling within a cortical column. J Physiol. 538:803–822.

Feldmeyer D, Roth A, Sakmann B. 2005. Monosynaptic connections between pairs of spiny stellate cells in layer 4 and pyramidal cells in layer 5A indicate that lemniscal and paralemniscal afferent pathways converge in the infragranular somatosensory cortex. J Neurosci. 25:3423–3431.

Frick A, Feldmeyer D, Sakmann B. 2007. Postnatal development of synaptic transmission in local networks of L5A pyramidal neurons in rat somatosensory cortex. J Physiol. 585:103–116.

Gidon A, Segev I. 2012. Principles governing the operation of synaptic inhibition in dendrites. Neuron. 75:330–341.

Gupta A, Wang Y, Markram H. 2000. Organizing principles for a diversity of GABAergic interneurons and synapses in the neocortex. Science. 287:273–278.

Helmstaedter M, de Kock CP, Feldmeyer D, Bruno RM, Sakmann B. 2007. Reconstruction of an average cortical column in silico. Brain Res Rev. 55:193–203.

Helmstaedter M, Sakmann B, Feldmeyer D. 2009a. L2/3 Interneuron groups defined by multiparameter analysis of axonal projection, dendritic geometry, and electrical excitability. Cereb Cortex. 19:951–962.

Helmstaedter M, Sakmann B, Feldmeyer D. 2009b. Neuronal correlates of local, lateral and translaminar inhibition with reference to cortical columns. Cereb Cortex. 19:926–937.

Helmstaedter M, Staiger JF, Sakmann B, Feldmeyer D. 2008. Efficient recruitment of layer 2/3 interneurons by layer 4 input in single columns of rat somatosensory cortex. J Neurosci. 28:8273–8284.

Hines ML, Carnevale NT. 1997. The NEURON simulation environment. Neural Comput. 9:1179–1209.

Holmgren C, Harkany T, Svennenfors B, Zilberter Y. 2003. Pyramidal cell communication within local networks in layer 2/3 of rat neocortex. J Physiol. 551:139–153.

Isaacson JS, Scanziani M. 2011. How inhibition shapes cortical activity. Neuron. 72:231–243.

Jadi M, Polsky A, Schiller J, Mel BW. 2012. Location-dependent effects of inhibition on local spiking in pyramidal neuron dendrites. PLoS Comput Biol. 8:e1002550.

Karube F, Kubota Y, Kawaguchi Y. 2004. Axon branching and synaptic bouton phenotypes in GABAergic nonpyramidal cell subtypes. J Neurosci. 24:2853–2865.

Keren N, Peled N, Korngreen A. 2005. Constraining compartmental models using multiple voltage recordings and genetic algorithms. J Neurophysiol. 94:3730–3742.

Kerr JN, de Kock CP, Greenberg DS, Bruno RM, Sakmann B, Helmchen F. 2007. Spatial organization of neuronal population responses in layer 2/3 of rat barrel cortex. J Neurosci. 27:13316–13328.

Koch C. 1999. Biophysics of computation. Oxford, New York: Oxford University Press.

Larkum ME, Zhu JJ, Sakmann B. 1999. A new cellular mechanism for coupling inputs arriving at different cortical layers. Nature. 398:338–341.

Liu BH, Li YT, Ma WP, Pan CJ, Zhang LI, Tao HW. 2011. Broad inhibition sharpens orientation selectivity by expanding input dynamic range in mouse simple cells. Neuron. 71: 542–554.

Llinas R, Nicholson C, Freeman JA, Hillman DE. 1968. Dendritic spikes and their inhibition in alligator Purkinje cells. Science. 160:1132–1135.

London M, Hausser M. 2005. Dendritic computation. Ann Rev Neurosci. 28:503–532.

Lübke J, Egger V, Sakmann B, Feldmeyer D. 2000. Columnar organization of dendrites and axons of single and synaptically coupled excitatory spiny neurons in layer 4 of the rat barrel cortex. J Neurosci. 20:5300–5311.

Lübke J, Roth A, Feldmeyer D, Sakmann B. 2003. Morphometric analysis of the columnar innervation domain of neurons connecting layer 4 and layer 2/3 of juvenile rat barrel cortex. Cereb Cortex. 13:1051–1063.

Markram H, Toledo-Rodriguez M, Wang Y, Gupta A, Silberberg G, Wu C. 2004. Interneurons of the neocortical inhibitory system. Nat Rev Neurosci. 5:793–807.

Meyer HS, Schwarz D, Wimmer VC, Schmitt AC, Kerr JN, Sakmann B, Helmstaedter M. 2011. Inhibitory interneurons in a cortical column form hot zones of inhibition in layers 2 and 5A. Proc Natl Acad Sci USA. 108:16807–16812.

Meyer HS, Wimmer VC, Oberlaender M, de Kock CP, Sakmann B, Helmstaedter M. 2010. Number and laminar distribution of neurons in a thalamocortical projection column of rat vibrissal cortex. Cereb Cortex. 20:2277–2286.

Miles R, Toth K, Gulyas AI, Hajos N, Freund TF. 1996. Differences between somatic and dendritic inhibition in the hippocampus. Neuron. 16:815–823.

Nicoll A, Kim HG, Connors BW. 1996. Laminar origins of inhibitory synaptic inputs to pyramidal neurons of the rat neocortex. J Physiol. 497(Pt 1):109–117.

Otsuka T, Kawaguchi Y. 2009. Cortical inhibitory cell types differentially form intralaminar and interlaminar subnetworks with excitatory neurons. J Neurosci. 29:10533–10540.

Packer AM, Yuste R. 2011. Dense, unspecific connectivity of neocortical parvalbumin-positive interneurons: a canonical microcircuit for inhibition? J Neurosci. 31:13260–13271.

Perrais D, Ropert N. 1999. Effect of zolpidem on miniature IPSCs and occupancy of postsynaptic GABAA receptors in central synapses. J Neurosci. 19:578–588.

Petersen CC, Hahn TT, Mehta M, Grinvald A, Sakmann B. 2003. Interaction of sensory responses with spontaneous depolarization in layer 2/3 barrel cortex. Proc Natl Acad Sci USA. 100:13638–13643.

Pfeffer CK, Xue M, He M, Huang ZJ, Scanziani M. 2013. Inhibition of inhibition in visual cortex: the logic of connections between molecularly distinct interneurons. Nat Neurosci. 16:1068–1076.

Pollak GD, Burger RM, Park TJ, Klug A, Bauer EE. 2002. Roles of inhibition for transforming binaural properties in the brainstem auditory system. Hear Res. 168:60–78.

Poo C, Isaacson JS. 2009. Odor representations in olfactory cortex: “sparse” coding, global inhibition, and oscillations. Neuron. 62:850–861.

Rall W. 1964. Theoretical significance of dendritic tree for input-output relation. In: Reiss RF, editor. Neural theory and modeling. Stanford (CA): Stanford University Press, p. 73–97.

Reyes A, Lujan R, Rozov A, Burnashev N, Somogyi P, Sakmann B. 1998. Target-cell-specific facilitation and depression in neocortical circuits. Nat Neurosci. 1:279–285.

Rose D, Blakemore C. 1974. Effects of bicuculline on functions of inhibition in visual cortex. Nature. 249:375–377.

Sarid L, Bruno R, Sakmann B, Segev I, Feldmeyer D. 2007. Modeling a layer 4-to-layer 2/3 module of a single column in rat neocortex: interweaving in vitro and in vivo experimental observations. Proc Natl Acad Sci USA. 104:16353–16358.

Sarid L, Feldmeyer D, Gidon A, Sakmann B, Segev I. 2013. Contribution of intracolumnar layer 2/3-to-layer 2/3 excitatory connections in shaping the response to whisker deflection in rat barrel cortex. Cereb Cortex. 25:849–858.

Schaefer AT, Helmstaedter M, Sakmann B, Korngreen A. 2003. Correction of conductance measurements in non-space-clamped structures: 1. Voltage-gated K^+ channels. Biophys J. 84:3508–3528.

Schaefer AT, Helmstaedter M, Schmitt AC, Bar-Yehuda D, Almog M, Ben-Porat H, Sakmann B, Korngreen A. 2007. Dendritic voltage-gated K^+ conductance gradient in pyramidal neurones of neocortical layer 5B from rats. J Physiol. 579:737–752.

Sillito AM. 1975. The contribution of inhibitory mechanisms to the receptive field properties of neurones in the striate cortex of the cat. J Physiol. 250:305–329.

Silver RA, Lübke J, Sakmann B, Feldmeyer D. 2003. High-probability uniquantal transmission at excitatory synapses in barrel cortex. Science. 302:1981–1984.

Stratford K, Mason A, Larkman AU, Major G, Jack JJB. 1989. The modelling of pyramidal neurones in the visual cortex. In: Durbin R., Miall C.G.M., editors. The Computing Neuron Wokingham. Addison-Wesley, p. 296–321.

Stuart GJ, Dodt HU, Sakmann B. 1993. Patch-clamp recordings from the soma and dendrites of neurons in brain slices using infrared video microscopy. Pflugers Arch. 423:511–518.

Tamas G, Buhl EH, Somogyi P. 1997. Fast IPSPs elicited via multiple synaptic release sites by different types of GABAergic neurone in the cat visual cortex. J Physiol. 500(Pt 3):715–738.

Thomson AM, West DC, Hahn J, Deuchars J. 1996. Single axon IPSPs elicited in pyramidal cells by three classes of interneurones in slices of rat neocortex. J Physiol. 496(Pt 1):81–102.

Thomson AM, West DC, Wang Y, Bannister AP. 2002. Synaptic connections and small circuits involving excitatory and inhibitory neurons in layers 2–5 of adult rat and cat neocortex: triple intracellular recordings and biocytin labelling in vitro. Cereb Cortex. 12:936–953.

Trevelyan AJ, Jack J. 2002. Detailed passive cable models of layer 2/3 pyramidal cells in rat visual cortex at different temperatures. J Physiol. 539:623–636.

Waters J, Helmchen F. 2006. Background synaptic activity is sparse in neocortex. J Neurosci. 26:8267–8277.

Wu GK, Arbuckle R, Liu BH, Tao HW, Zhang LI. 2008. Lateral sharpening of cortical frequency tuning by approximately balanced inhibition. Neuron. 58:132–143.

Xu X, Callaway EM. 2009. Laminar specificity of functional input to distinct types of inhibitory cortical neurons. J Neurosci. 29:70–85.